
Plasmonic Properties of Aluminium Nanocylinders in the Visible Range

Gillibert Raymond^{1,2}, Colas Florent³, Yasukuni Ryohei¹, Picardi Gennaro¹,
Lamy de la Chapelle Marc^{1,*}

¹ Université Paris 13, Sorbonne Paris Cité, Laboratoire CSPBAT, CNRS, (UMR 7244), 74 rue Marcel Cachin, F-93017 Bobigny, France,

² HORIBA Jobin Yvon S.A.S. 231 rue de Lille 59650 Villeneuve d'Ascq, France

³ Laboratoire Ditection, Capteurs et Mesures, Centre Bretagne - ZI de la Pointe du Diable - CS 10070 - 29280 Plouzané, France

* Corresponding author : Marc Lamy de la Chapelle, email address :
marc.lamydelachapelle@univ-paris13.fr

Abstract :

Plasmonic and surface enhanced Raman scattering (SERS) studies have been performed on aluminium nanocylinders arrays of different diameters. We observed sharp localised surface plasmon resonance (LSPR) peaks that can be tuned on the whole visible range and having the same behaviour than gold nanocylinders. The near-field enhancement was measured by SERS on probe molecules as well as on the indium tin oxide (ITO) substrate using two excitation wavelengths: 660 and 785 nm. No SERS signal of the probe molecule

Introduction

Aluminium as plasmonic material has attracted considerable attention in the recent years and several plasmonic studies have been performed on aluminium nanostructures. Indeed, the real part of the Al dielectric constant is strongly negative and allows having a plasmon resonance from the ultra-violet to the far infra-red. As a consequence, the aluminium appears to be usable in plasmonics on a very wide spectral range. Moreover, its price is very low compared to gold or silver usually used in plasmonic devices which make Al a good candidate to reduce the cost of such systems for mass production. Plasmonic studies were conducted by C. Langhammer *et al.*¹ on aluminium nanocylinders randomly distributed on a glass slide. Those substrates showed a tuneable resonance position depending on the disk diameter. It was also shown that a thin alumina oxide layer of a few nanometers is quickly formed at the surface of the structures, its thickness slowly growing with time. The potential applications of such nanostructures to surface enhanced spectroscopy have also been studied. For instances,

1
2
3 in 2007, C. Zhang *et al.*² designed an aluminium substrate for surface enhanced Raman
4 scattering (SERS) produced by anodisation and the SERS signal of protein and bacteria
5 were recorded with a 514 nm laser line. Later, a strong SERS signal of crystal violet has
6 been reported on a simple aluminium sputtered surface with a UV excitation (244 nm) by T.
7 Dörfer *et al.*³ More recently, B. Cerjan *et al.*⁴ demonstrated the application of Al asymmetric
8 nanoantenna in surface enhanced IR absorption (SEIRA) taking advantage of the alumina
9 oxide layer to graft molecules at the nanoantenna surface. It is also known that the imaginary
10 part of the Al dielectric constant exhibits a large absorption close to 800 nm that could induce
11 a decrease of the plasmonics performances due to large damping of the plasmon resonance.
12 However, in the studies performed by C. Langhammer *et al.*,¹ sharp plasmonic resonances
13 were obtained in the near infra-red (NIR) indicating a potential for near-field enhancement
14 in this spectral region. In this framework, we present a far-field and a near-field study of
15 periodic aluminium nanocylinders arrays with different diameters. Those samples featured
16 localised surface plasmon resonances that could be tuned from UV to NIR. We also observe
17 multiple orders of resonance as well as strong Wood's anomalies in the plasmon excitation.
18 The Wood anomalies are related to the Fano resonance coming from the interference of the
19 plasmon mode of the nanocylinders and the grating modes of the array of nanocylinder.⁵
20 SERS was equally performed to quantify the near-field enhancement of those structures.
21 Despite the high quality factor plasmonic resonators, we could not achieve a very high SERS
22 activity. Advanced DDA calculations demonstrated that such structures could provide only
23 limited near-field enhancement not sufficient for most of the SERS applications and not
24 comparable to gold nanostructures even if their far-field optical properties are similar.
25
26
27
28
29
30
31
32
33
34
35
36
37
38
39
40
41
42
43
44
45
46
47
48
49
50
51
52
53
54
55
56
57
58
59
60

Experimental and Theoretical Methods

Experimental

Square array of aluminium nanocylinders were fabricated by electron beam lithography in clean room. On top of a commercial 0.7 mm thick glass slide already covered with a 160 nm thick indium tin oxide (ITO) layer, a 140 nm thick Poly(methyl methacrylate) (PMMA) layer was deposited by spin coating. The PMMA layer was exposed with an electron beam using a ZEISS scanning electron microscope. The PMMA development was then done for 40 s in a standard 1:3 methyl isobutyl ketone / isopropanol (MIBK/IPA) solution. An aluminium layer of 30 nm was then deposited on the substrate. Finally a lift-off process was performed for one night in acetone to remove the PMMA.

The nanocylinder height was fixed to 30 nm and the nanocylinder diameters were varied from 50 to 250 nm by a 10 nm step. A gap of 200 nm was kept constant between the nanocylinders to avoid any near-field coupling. The quality of our nanostructures was verified by scanning electron microscopy in order to determine their exact sizes (figure 1).

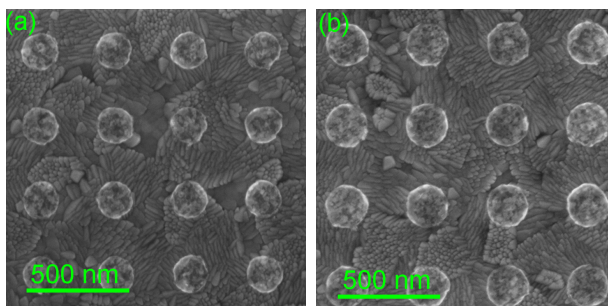


Figure 1: SEM images of arrays of aluminium nanocylinders produced by electron beam lithography for diameter of (a) 180 nm and (b) 205 nm. The disks are deposited on a ITO coated glass substrate.

Extinction and SERS measurements were performed with an XploRA confocal Raman micro spectrometer (Horiba Scientific). For extinction measurements a non polarised white lamp was used to excite the nanocylinders and the transmitted light was collected with a 10 \times magnification objective (numerical aperture of 0.25) after removing the edge filters inside the

1
2
3 Raman spectrometer. For SERS, the Raman spectra were recorded with 660 nm and 785 nm
4 excitations wavelengths in backscattering configuration using a 100× magnification objective
5 (numerical aperture of 0.90). The laser power was adjusted to 300 μ W with neutral density
6 filter.
7
8
9

10
11 To measure the SERS signal, several probe molecules were chosen because of their high
12 Raman cross-section. These molecules are thiophenol (TP), 1,2-di(4-pyridyl)ethylene (BPE)
13 and methylene blue (MB). After UV-Ozone treatment the probe molecules were adsorbed on
14 the nanocylinder samples sequentially. We started with the TP and finished with the MB.
15 For all these probe molecules, the samples were immersed in a 1 mM concentrated solution
16 in ethanol for 1 hour and then dried. For each probe molecule, five Raman spectra were
17 measured at different locations randomly distributed on each nanocylinder array. An average
18 intensity was calculated by using the five Raman spectra and the standard deviation was
19 used as error bar.
20
21
22
23
24
25
26
27
28
29
30
31

32 Modeling

33
34 The electric field calculation was performed by DDA (Discrete Dipole Approximation)⁶ using
35 DDSCAT 7.3.^{7,8} The shape of the nanoparticles was generated by a home-made code written
36 in Python. It consisted in arrays of nanocylinders of diameters going from 100 nm to 260 nm
37 by a 20 nm step. Their upper corner had been rounded with a radius of curvature of 6 nm to
38 take into account the imperfection of the lift-off process. The nanocylinders were arranged in
39 a square lattice. The inter-particle spacing was set to 200 nm.
40
41
42
43
44
45
46

47 The nanoparticle was discretized by dipoles separated by a distance of 1 nm. The
48 polarizability of each dipole was calculated by the filtered dipole as suggested by Piller and
49 Martin.⁹ The inversion was carried out by biconjugate gradient with stabilization algorithm
50 as proposed by Sleijpen and van der Vorst.¹⁰ Calculation was performed in double precision
51 on the high performance calculation facilities PCIM (*Pole Calcul Intensif pour la Mer*). The
52 convergence tolerance was set to 10⁻⁷. The nanoparticle was considered in an effective medium
53
54
55
56
57
58
59
60

of relative permittivity as the mean of that of air and of ITO (Indium Tin Oxide). The former was considered constant and equal to 1 while the latter was measured by ellipsometry. The relative permittivity came from the paper of Rakić.¹¹

The effect of a thin layer of alumina oxide (Al_2O_3) around the nanocylinders was investigated following the approach proposed by Knight et al..¹² As the oxide layer appears the nanocylinders was considered as a mixture of oxide and aluminium whose relative permittivity was calculated with the Bruggeman model. The oxide refractive index was taken from¹³ (see supplementary information). The near-field features of the nanocylinders were calculated by averaging the electric-field in a shell of 1 nm thickness around the nanocylinders. This quantity is noted $\langle E^2 \rangle$ hereafter.

Results and discussion

Extinction analysis

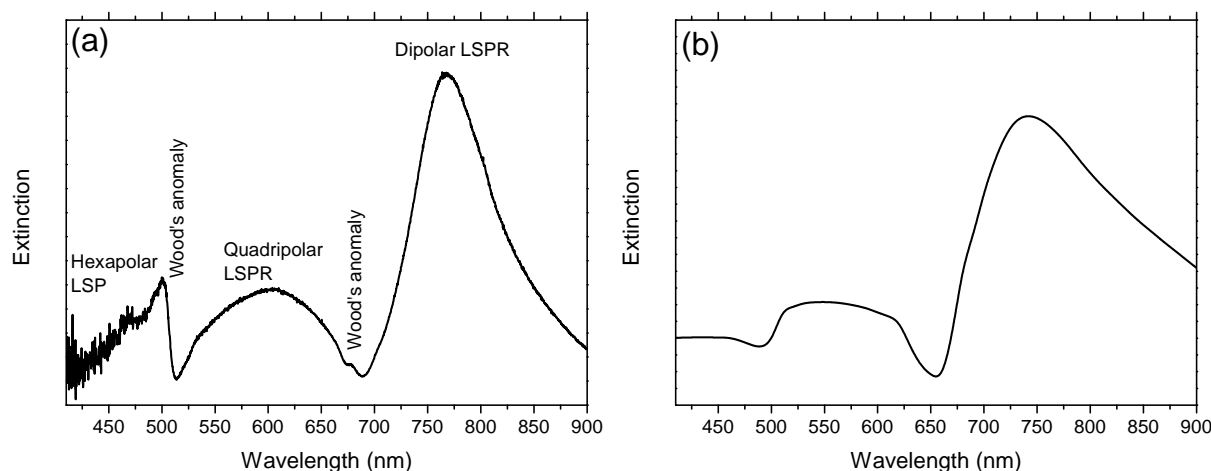


Figure 2: (a) Experimental and (b) simulated extinction spectra for nanocylinders array with diameter of 250 nm.

The day after the nanocylinder production, the extinction spectrum of each nanocylinder diameter were recorded. The experimental extinction spectrum of 250 nm diameter nanocylinders is shown on figure 2a. It exhibits an intense dipolar mode at 770 nm as well as bands

1
2
3
4 at lower wavelengths that could be assigned to higher orders of resonance (quadripolar and
5 hexapolar modes). These latter bands are observable only for large diameters (higher than
6 80 nm for quadripolar mode and 210 nm for hexapolar one). LSPR position is plotted as
7 a function of the nanocylinders diameter on figure 3. As expected, whatever the order of
8 resonance is, the LSPR position red-shifts when the diameter monotonically increases as
9 already observed for gold nanocylinders.¹⁴

10
11
12
13
14
15
16 The simulated extinction spectrum for nanocylinder diameter of 250 nm is shown in
17 figure 2b. One can notice a very good agreement with the experimental spectrum and the
18 simulation reproduces the different LSP modes. Such agreement is observable for all diameters
19 as shown by the comparison of the simulated and experimental LSP positions on figure 3.

20
21
22
23
24 The dipolar mode exhibits an asymmetric band shape because of the inter-band transitions
25 of aluminium close to 800 nm (maximum of the imaginary part of the Al dielectric constant,
26 figure 4). In the spectral range of the inter-band transitions, the damping of the plasmon
27 increases and the extinction band broadens. The LSPR asymmetry is amplified by the
28 Wood's anomaly observable as a drop of the extinction intensity on the low wavelength side
29 of the LSPR. This anomaly is due to far field coupling between the individual nanocylinders
30 through the array.¹⁵ The Wood's anomaly is clearly observable with those structures because
31 of the ITO coating. Indeed, this latter one could induce the apparition of a guided mode
32 at the substrate surface that amplifies the coupling between the nanostructures and as a
33 consequence the Wood's anomaly observation. Very similar phenomenon was described by A.
34 Christ et al.¹⁶

35
36
37
38
39
40
41
42
43
44
45
46 The LSPR broadening can be observed on figure 3 as the full width at half maximum of
47 the dipolar mode is plotted as a function of its position. One can notice that the dipolar
48 mode can be very thin (width lower than 50 nm) and that the width increases strongly when
49 the resonance becomes closer to the inter-band transitions at 800 nm. This result is consistent
50 with the intrinsic property of the aluminum.¹⁷ However, the widths are still comparable or
51 even thinner than the ones measured for gold nanocylinders.¹⁸⁻²⁰ This is actually remarkable
52
53
54
55
56
57
58
59
60

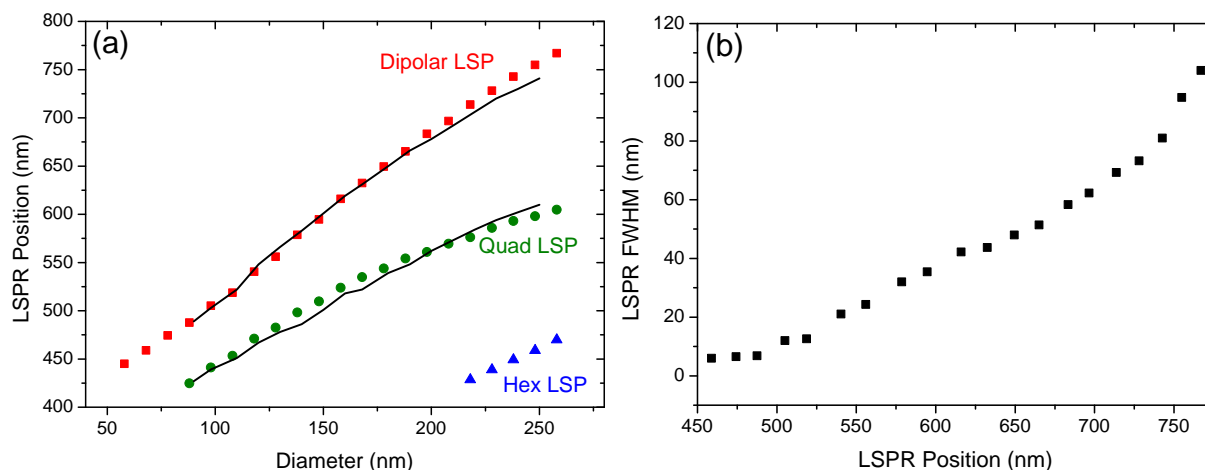


Figure 3: (a) LSPs position as a function of nanocylinders diameters. Dots correspond to the experimental measurements (red squares: dipolar mode, green dots: quadrupolar mode, blue triangle: hexapolar mode) whereas the black lines correspond to DDA simulations. (b) Full width at half maximum of the dipolar mode as a function of the dipolar mode position.

since the imaginary part of Al is largely higher than the one of Au (between 10 and 50 times higher on the 600-900 nm range). This property could be exploited in sensors based on the observation of the LSPR shift due to the adsorption of molecules at the nanostructure surface and could confer to such systems a very high sensitivity

Moreover, the bandwidth has a direct influence on the Q-factor of the resonance. As previously demonstrated,^{18,21} a thinner LSPR band and as a consequence a larger the Q-factor of the plasmon resonator induces a greater near-field enhancement.

In the quasi-static approximation, Wang and Shen²² demonstrated that the quality (Q) factor of the LSPR is given by:

$$Q = \omega \frac{\frac{\partial \epsilon_r}{\partial \omega}(\omega)}{2(\epsilon_i(\omega))^2} \quad (1)$$

where ϵ_r and ϵ_i are the real and the imaginary parts of the dielectric constant of the material and ω is the pulsation. The application of this formula shows that in the visible range, the Q factor of aluminum nanoparticles is very low (lower than 0.5 for wavelength higher than 500 nm and nearly null around 800 nm, fig.4a)¹⁷ whereas for gold, the Q factor is above 5 in the visible range and up to 25 for wavelength around 700 nm. This is due to

the largely higher imaginary part of the Al compared to Au in the visible range.

However, the Q-factor calculated experimentally from the extinction spectrum of Al nanocylinders can take values up to 70 for wavelengths lower than 500 nm (figure 5), which is of the same order of magnitude than for gold nanoparticles. The Q-factor decreases with the wavelength as the LSPR becomes closer to the inter-band transitions but is still higher than 5. This actually differs very much from the quasi-static approximation calculation probably thanks to the far-field coupling of LSPR with the grating, sharpening the extinction band and also to the fact that quasi-static approximation cannot be actually applied for big structures. In fact, the sharpening of the plasmon bands can be explained by two different effects: the far-field coupling of the nanocylinders^{5,23-25} and the Wood's anomalies. In the former case, the coupling leads to a reduction of the Full-Width at Half Maximum of the extinction band. In the latter case, the Wood's anomaly is always located slightly blue shifted compared to the LSPR, inducing a possible coupling between those two modes and a supplementary sharpening of the LSPR. Thus, although the poor optical properties of alumina in the red, far-field properties of nanocylinders leads us to expect strong local field enhancement and then SERS detection capabilities even in the NIR region, when plasmon resonance is close to the inter-band transitions.

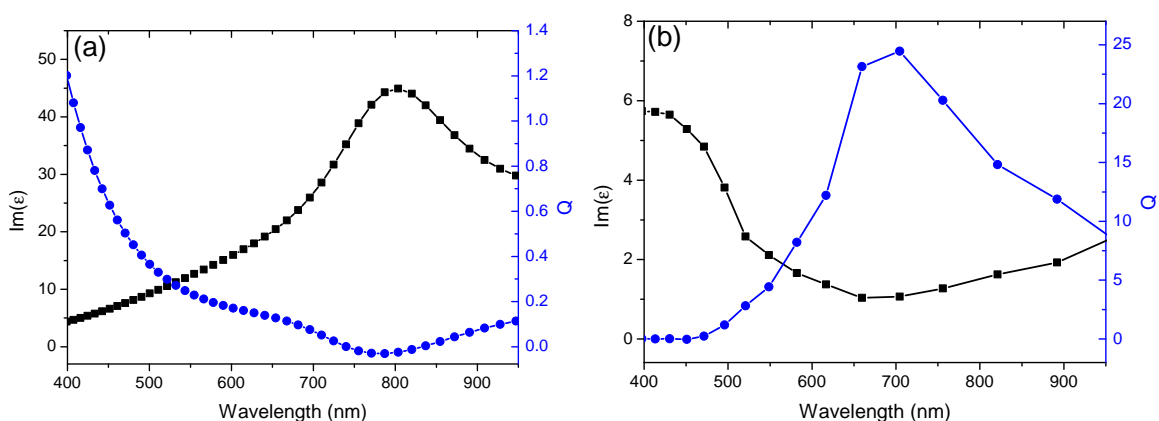


Figure 4: Imaginary part of the dielectric constant of Aluminium (black squares, left axis) and Q-factor in the quasi-static approximation (blue circles, right axis) with refractive index from Rakić 1998. (b) Same for gold with refractive index from Johnson and Christy.

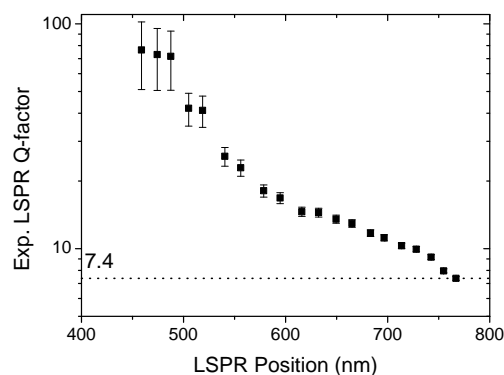


Figure 5: Experimental Q-factor calculated from the extinction spectra of the Al nanocylinders as a function of the LSPR position.

SERS Analysis

Several probe molecules were deposited sequentially at the surface of the nanocylinders (1st TP, 2nd BPE and 3rd MB) and SERS spectra were acquired at 660 nm and 785 nm excitation wavelengths for each nanocylinders diameter. For all diameters, none of the specific Raman bands of TP, BPE or MB were observed on the SERS spectrum as shown on figure 6a. This can be due to two distinct reasons. First, one can assume that the molecules cannot graft or adsorb at the nanocylinder surface and as a consequence, are not present at the surface of the nanocylinders during the SERS experiments. Second, the aluminium oxide layer prevented the molecules from attaining the near-field enhanced region. The oxide plays the role of a spacer layer between the molecules and the metallic surface. In both cases, we could not observe any SERS spectrum from the probe molecules that limit considerably the use of such metal for SERS.

However some Raman features in the low frequency range between 300 and 700 cm^{-1} can be observed, corresponding to the ITO substrate (figure 6). The intensity of these bands is enhanced in the presence of the nanocylinders and we used them to quantify the SERS enhancement. In figures 6(b) and 6(c), is shown the integrated SERS intensity from 300 to 700 cm^{-1} for 660 nm and 785 nm excitation wavelengths as a function of the LSPR positions. We observe a strong variation of the SERS signal when we tune the LSPR with a maximum

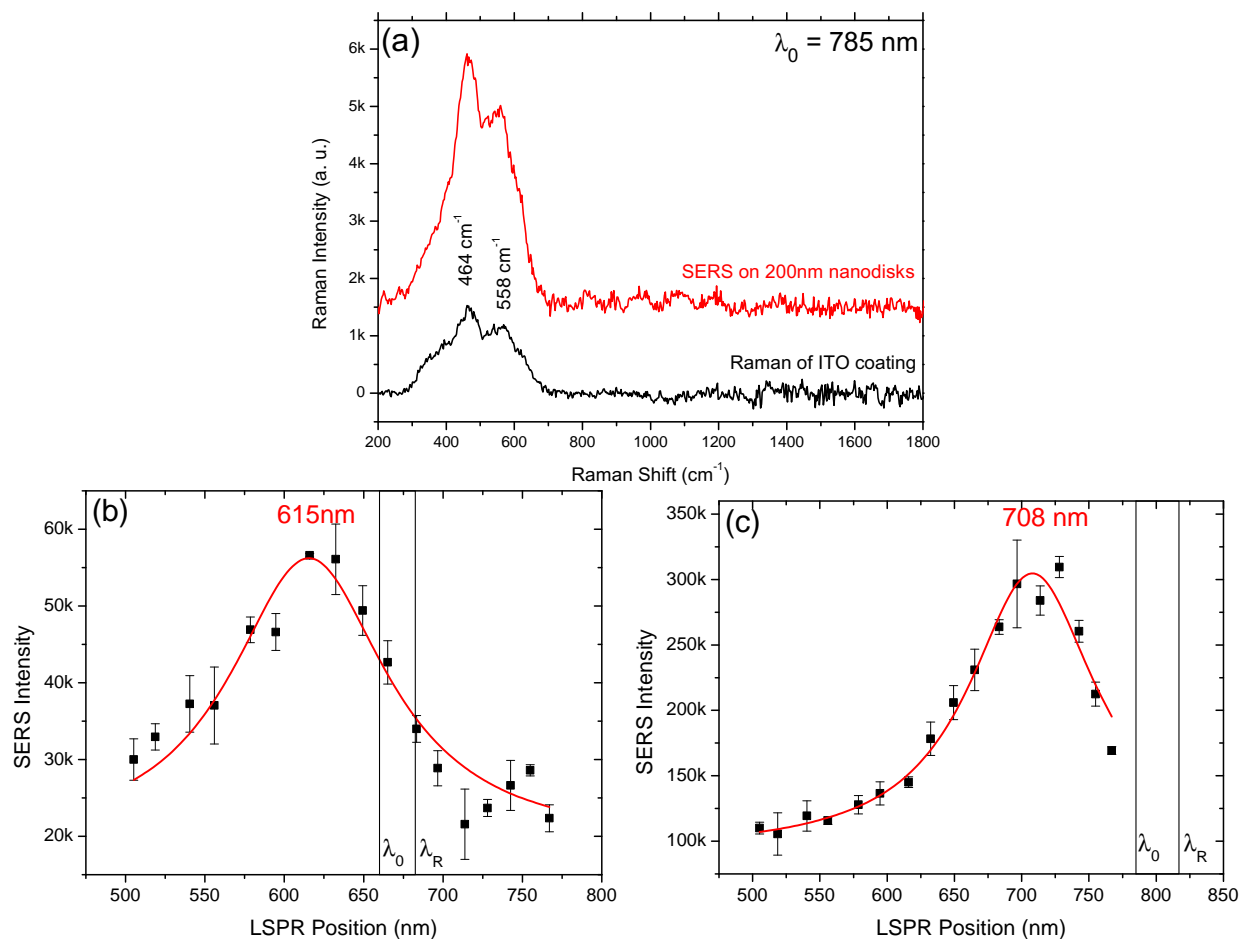


Figure 6: (a) Raman spectra on ITO coating and on nanocylinders array with the 785 nm excitation wavelength and SERS intensity as a function of the LSPR position for (b) 660 nm and (c) 785 nm excitation wavelengths. The black vertical lines correspond to the position of the excitation and Raman wavelengths (λ_0 and λ_R respectively).

of intensity at a specific LSPR. However, the SERS efficiency is lower than the one observed for gold since the ratio between the highest and the lowest signals is between 2 and 3 for Al whereas it is more than 10 for Au.¹⁸ In addition, when we compare the size of the laser spot and the area of the nanocylinders, an enhancement less than 15 can be calculated in the case of the 200 nm diameter nanocylinders excited at 785 nm. It is definitely much lower than typical SERS enhancement achieved with gold nanocylinders.²⁶

This lower near-field enhancement with Al cannot be explained by a bad quality factor in this spectral range as we demonstrate in the previous section that the Q factor is high for our Al nanocylinders.

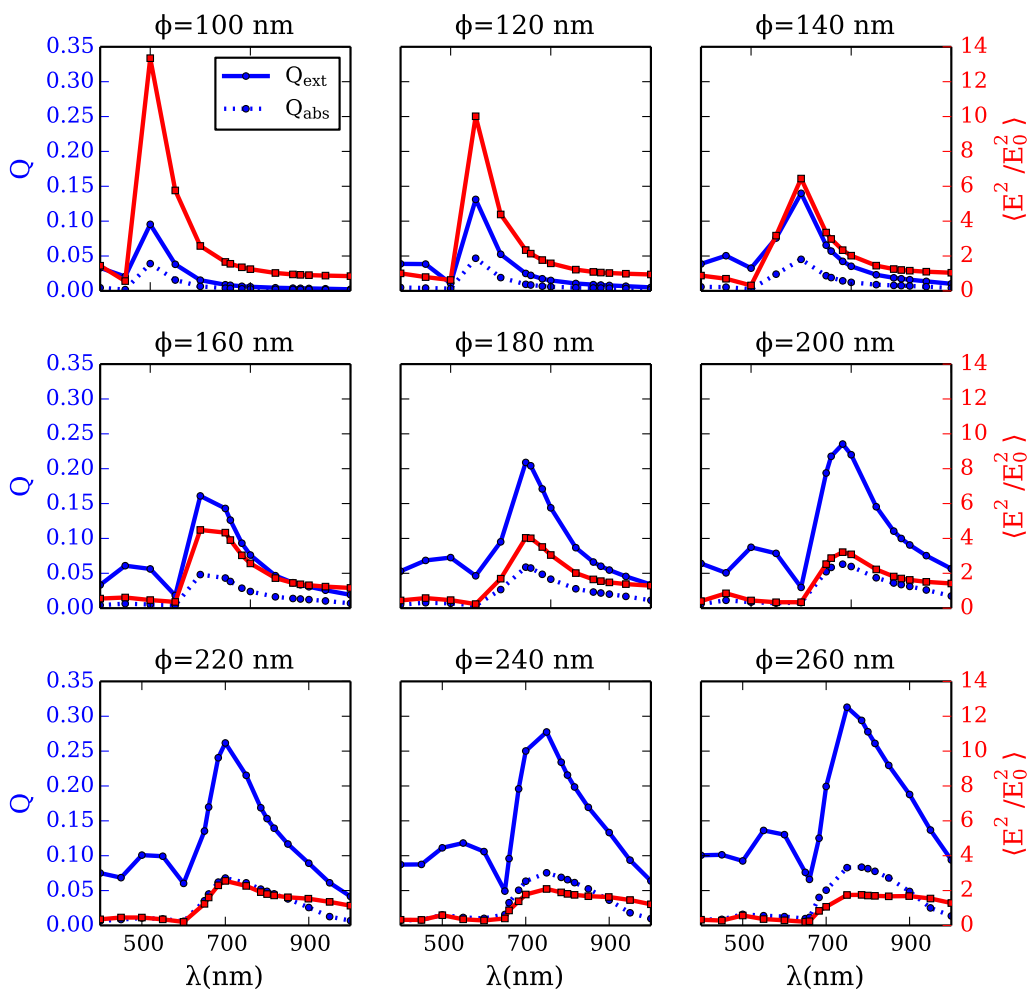


Figure 7: Near-Field feature of the Al nanocylinders: The near-field enhancement is plotted as $\langle E^2/E_0^2 \rangle$ (red curve and right axis), the extinction cross section (blue curve and left axis) and the absorption cross section (blue dotted curve and left axis) are plotted versus the wavelength depending on the nanocylinder diameter (Φ).

This is confirmed by the DDA calculation. The average electric field around the nanocylinders is plotted on fig. 7 for diameters ranging from 100 nm to 260 nm and superimposed with the absorption and the extinction cross-section. First, the maxima of the absorption and the extinction cross-sections increase with the LSPR wavelength. Second, the maximum value of $\langle E^2/E_0^2 \rangle$ decreases with the resonance wavelength, up to sevenfold when comparing the 100 nm and the 260 nm diameter nanocylinders. Third, for resonance wavelength larger than

1
2
3 700 nm, the near-field spectrum appears wide and flat. These three main features can be
4 explained by the inter-band transition. Indeed, the imaginary part of aluminium dielectric
5 constant increases monotonically in the 400-700 nm range (figure 4). It has two consequences:
6 first, an increase of the absorption and subsequently of the extinction cross-section, second, a
7 decrease of the local field. In addition, the absorption maximum of the alumina is around
8 800 nm and at this wavelength, the plasmon mode is strongly absorbed.
9

10
11 The comparison of fig. 7 with previous work by Colas et al.¹⁸ shows that in the 600-800 nm
12 domain $\langle E^2/E_0^2 \rangle$ is an order of magnitude lower than in the case of gold nanocylinders,¹⁸
13 which lead to a lower SERS enhancement with aluminum as experimentally observed.
14

15
16 Moreover, the optimum LSPR position is largely outside the spectral range λ_0, λ_R with
17 λ_0 the excitation wavelength and λ_R the Raman wavelength as the optimum LSPR positions
18 to maximise the SERS signal is located at 615 nm for a 660 nm excitation wavelength and at
19 708 nm for a 785 nm excitation (figure 6). Previous works demonstrated experimentally and
20 theoretically that the near-field can be red-shifted²⁷⁻³³ compared to the far-field resonance.
21 This shift can reach up to 200 nm in the case of nanoantenna resonating in the mid-IR.²⁹
22 However, figure 7 shows that the near-field is slightly shifted with regards to the far-field.
23 This is similar to a previous study considering gold and aluminium nanocylinders^{18,34} in
24 this spectral range. Indeed, the red-shift increases with the damping of the electron cloud
25 oscillation inside the nanocylinder.³¹ It can be characterized by the Full Width at Half
26 Maximum of the extinction bands. In the case of the nanocylinders, the FWHM increases
27 from 20 nm to 100 nm as the diameter goes from 100 to 240 nm. The losses associated with
28 the nanocylinders are then expected to be small¹⁸ and the near-field to far-field red-shift
29 subsequently low. Thus the assumption of a near-field to far-field shift cannot be considered
30 to explain our SERS results.
31

32
33 As we previously noted, the absolute value of the $\langle E^2/E_0^2 \rangle$ decreases and its band width
34 increases when the LSPR is red-shifted. For example, for the 100 nm nanocylinder, the
35 maximum value of $\langle E^2/E_0^2 \rangle$ is around 14 with a bandwidth of 100 nm whereas the maximum
36
37
38
39
40
41
42
43
44
45
46
47
48
49
50
51
52
53
54
55
56
57
58
59
60

1
2
3 value of $\langle E^2/E_0^2 \rangle$ is only 3 for a 200 nm nanocylinder with a bandwidth around 130 nm. Since
4 the SERS intensity is proportional to the average Single Molecule Enhancement Factor¹⁷
5 ($\langle SMEF \rangle$) defined by:
6
7
8

$$\langle SMEF \rangle \propto \int_V \frac{E(\lambda_0)^2 E(\lambda_R)^2}{E_0(\lambda_0)^4} dV \quad (2)$$

9
10
11 where $E(\lambda_0)$ and $E(\lambda_R)$ are electric fields around the nanocylinders at the excitation and
12 the Raman wavelengths respectively, E_0 is the incoming electric field and V is the volume in
13 which the calculation is carried out, the SERS intensity depends directly on the electric field
14 around the nanocylinders. From fig. 7 we can assume that the SERS enhancement will be
15 larger for the low resonance wavelengths even out of resonance compared to nanocylinders
16 having higher resonance wavelength. For example, in the case of $\lambda_0=660$ nm, $\langle E^2(\lambda_0)/E_0^2 \rangle$
17 is larger for a diameter of 160 nm than a diameter of 180 nm. However, the first resonates
18 at 618 nm while the second at 656 nm. This effect has already been observed and explained
19 with gold nanocylinders.¹⁸
20
21
22
23
24
25
26
27
28
29
30
31
32

33 In addition, aluminium absorbs light in the 700-900 nm domain because of the inter-band
34 transitions (Fig. 4). In this range, the electromagnetic energy is then converted to heat.³⁴
35 This thermal effect is assumed to reduce electromagnetic enhancement traditionally express
36 by eq. 2.
37
38
39
40

41 These two effects contribute to reach a larger SERS signal with nanocylinder resonating
42 at lower wavelengths and then to obtain an optimal LSPR position strongly blue shifted with
43 regards to the excitation and the Raman wavelengths. The near-field enhancement is largely
44 lower for Al than for Au as experimentally observed and this could also explain why we could
45 not detect any SERS signal from the probe molecules, especially with the presence of the
46 oxide layer at the nanocylinder surface.
47
48
49
50
51
52
53
54
55
56
57
58
59
60

Conclusion

Aluminium nanocylinders were produced by electron beam lithography and their optical properties were investigated. We demonstrate that the LSPR can be tuned on the whole visible range. A broadening of the LSPR line width is observed when the LSPR is redshifted due to the inter band transitions occurring close to 800 nm. We measured the near-field enhancement by SERS on probe molecules as well as on the ITO substrate. For the former ones no SERS signal was recorded due to very low enhancement and to the formation of the oxide layer. This means that such substrate could not be applied for SERS in this spectral range. The low enhancement is confirmed by the observation of the ITO SERS signal. The signal variation with the LSPR position is one order of magnitude lower than the one observed with gold. This enhancement is largely decreased when the LSPR is close to the inter band transition at 800 nm that results in a spectral shift between the SERS signal optimum and the LSPR position.

Supporting Information

Aeging study over two months of the aluminium nanocylinders arrays, using LSPR position.

Acknowledgement

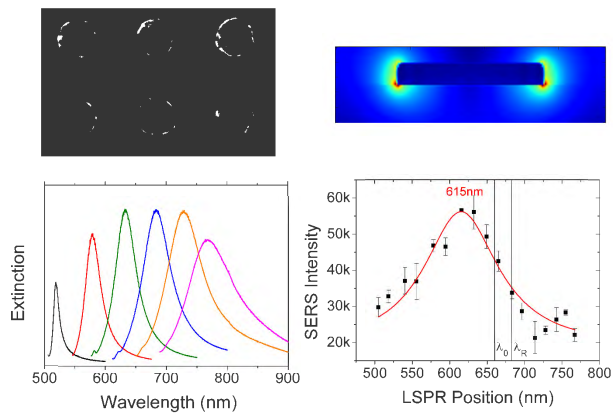
The authors thank Tina Odaka and Denis Croizé-Fillon for their kind and efficient advices and help with the high calculation facilities. Thanks to the *Centrale de Proximité en Nanotechnologies de Paris Nord (CPN2, 99 Avenue Jean-Baptiste Clément 93430 Villetaneuse, France)* to supply the clean room for samples fabrication. The authors also acknowledge ANR P2N (ANR-12-NANO-0016) and the support of the French Government and ANRT *Association Nationale de la Recherche et de la Technologie* for funding.

References

- (1) Langhammer, C.; Schwind, M.; Kasemo, B.; Zoric, I. Localized Surface Plasmon Resonances in Aluminum Nanodisks. *Nano Lett.* **2008**, *8*, 1461–1471.
- (2) Zhang, C.; Smirnov, A.; Hahn, D.; Grebel, H. Surface Enhanced Raman Scattering of Biospecies on Anodized Aluminum Oxide Films. *Chem. Phys. Lett.* **2007**, *440*, 239–243.
- (3) Dörfer, T.; Schmitt, M.; Popp, J. Deep-UV Surface-Enhanced Raman Scattering. *J. Raman Spectrosc.* **2007**, *38*, 1379–1382.
- (4) Cerjan, B.; Yang, X.; Nordlander, P.; Halas, N. J. Asymmetric Aluminum Antennas for Self-Calibrating Surface-Enhanced Infrared Absorption Spectroscopy. *ACS Photonics* **2016**, *3*, 354–360.
- (5) Hicks, E. M.; Zou, S.; Schatz, G. C.; Spears, K. G.; Van Duyne, R. P.; Gunnarsson, L.; Rindzevicius, T.; Kasemo, B.; Käll, M. Controlling Plasmon Line Shapes Through Diffractive Coupling in Linear Arrays of Cylindrical Nanoparticles Fabricated by Electron Beam Lithography. *Nano Lett.* **2005**, *5*, 1065–1070.
- (6) Purcell, E. M.; Pennypacker, C. R. Scattering and Absorption of Light by Nonspherical Dielectric Grains. *Astrophys. J.* **1973**, *186*, 705–714.
- (7) Draine, B. T.; Flatau, P. J. Discrete-Dipole Approximation for Periodic Targets: Theory and Tests. *J. Opt. Soc. Am. A* **2008**, *25*, 2693–2703.
- (8) Flatau, P. J.; Draine, B. T. Fast Near Field Calculations in the Discrete Dipole Approximation for Regular Rectilinear Grids. *Opt. Express* **2012**, *20*, 1247–1252.
- (9) Piller, N.; Martin, O. J. Increasing the Performance of the Coupled-Dipole Approximation: A Spectral Approach. *IEEE Trans. Antennas Propag.* **1998**, *46*, 1126–1137.
- (10) Sleijpen, G. L.; van der Vorst, H. A. Reliable Updated Residuals in Hybrid Bi-CG Methods. *Computing* **1996**, *56*, 141–163.
- (11) Rakić, A. D. Algorithm for the Determination of Intrinsic Optical Constants of Metal Films: Application to Aluminum. *Appl. Opt.* **1995**, *34*, 4755–4767.
- (12) Knight, M. W.; King, N. S.; Liu, L.; Everitt, H. O.; Nordlander, P.; Halas, N. J. Aluminum for Plasmonics. *ACS Nano* **2014**, *8*, 834–840, PMID: 24274662.

- 1
2
3
4 (13) Palik, E. *Handbook of Optical Constants of Solids II*; Academic Press handbook series; Academic Press,
5 1991.
6
7
8 (14) Zorić, I.; Zäch, M.; Kasemo, B.; Langhammer, C. Gold, Platinum, and Aluminum Nanodisk Plasmons:
9 Material Independence, Subradiance, and Damping Mechanisms. *ACS Nano* **2011**, *5*, 2535–2546, PMID:
10 21438568.
11
12
13 (15) Haynes, C. L.; McFarland, A. D.; Zhao, L.; Van Duyne, R. P.; Schatz, G. C.; Gunnarsson, L.; Prikulis, J.;
14 Kasemo, B.; Käll, M. Nanoparticle Optics: The Importance of Radiative Dipole Coupling in Two-
15 Dimensional Nanoparticle Arrays. *J. Phys. Chem. B* **2003**, *107*, 7337–7342.
16
17
18 (16) Christ, A.; Tikhodeev, S.; Gippius, N.; Kuhl, J.; Giessen, H. Waveguide-Plasmon Polaritons: Strong
19 Coupling of Photonic and Electronic Resonances in a Metallic Photonic Crystal Slab. *Phys. Rev. Lett.*
20 **2003**, *91*, 183901.
21
22
23 (17) Le Ru, E. C.; Etchegoin, P. G. In *Principles of Surface-Enhanced Raman Spectroscopy*; Le Ru, E. C.,
24 Etchegoin, P. G., Eds.; Elsevier: Amsterdam, 2009; pp 121–183.
25
26
27 (18) Colas, F. J.; Cottat, M.; Gillibert, R.; Guillot, N.; Djaker, N.; Lidgi-Guigui, N.; Toury, T.; Barchiesi, D.;
28 Toma, A.; Di Fabrizio, E. et al. Red-Shift Effects in Surface Enhanced Raman Spectroscopy: Spectral
29 or Intensity Dependence of the Near-Field? *J. Phys. Chem. C* **2016**, *120*, 13675–13683.
30
31
32 (19) Lamy de la Chapelle, M.; Shen, H.; Guillot, N.; Frémaux, B.; Guelorget, B.; Toury, T. New Gold
33 Nanoparticles Adhesion Process Opening the Way of Improved and Highly Sensitive Plasmonics
34 Technologies. *Plasmonics* **2013**, *8*, 411–415.
35
36
37 (20) Shen, H.; Guillot, N.; Rouxel, J.; Lamy de la Chapelle, M.; Toury, T. Optimized Plasmonic Nanostruc-
38 tures for Improved Sensing Activities. *Opt. Express* **2012**, *20*, 21278–21290.
39
40
41 (21) Colas, F.; Barchiesi, D.; Kessentini, S.; Toury, T.; Lamy de la Chapelle, M. Comparison of Adhesion
42 Layers of Gold on Silicate Glasses for SERS Detection. *J. Opt.* **2015**, *17*, 114010.
43
44
45 (22) Wang, F.; Shen, Y. R. General Properties of Local Plasmons in Metal Nanostructures. *Phys. Rev. Lett.*
46 **2006**, *97*, 206806.
47
48
49 (23) Meier, M.; Wokaun, A.; Liao, P. F. Enhanced Fields on Rough Surfaces: Dipolar Interactions Among
50 Particles of Sizes Exceeding the Rayleigh Limit. *J. Opt. Soc. Am. B* **1985**, *2*, 931–949.
51
52
53
54
55
56
57
58
59
60

- 1
2
3
4 (24) Carron, K. T.; Fluhr, W.; Meier, M.; Wokaun, A.; Lehmann, H. W. Resonances of Two-Dimensional
5 Particle Gratings in Surface-Enhanced Raman Scattering. *J. Opt. Soc. Am. B* **1986**, *3*, 430–440.
6
7
8 (25) Félidj, N.; Laurent, G.; Aubard, J.; Lévi, G.; Hohenau, A.; Krenn, J. R.; Aussenegg, F. R. Grating-
9 Induced Plasmon Mode in Gold Nanoparticle Arrays. *J. Chem. Phys.* **2005**, *123*, 221103.
10
11
12 (26) David, C.; Guillot, N.; Shen, H.; Toury, T.; Lamy de la Chapelle, M. SERS Detection of Biomolecules
13 Using Lithographed Nanoparticles Towards a Reproducible SERS Biosensor. *Nanotechnology* **2010**, *21*,
14 475501.
15
16
17
18 (27) Ross, B. M.; Lee, L. P. Comparison of Near- and Far-Field Measures for Plasmon Resonance of Metallic
19 Nanoparticles. *Opt. Lett.* **2009**, *34*, 896–898.
20
21
22 (28) Kelly, K. L.; Coronado, E.; Zhao, L. L.; Schatz, G. C. The Optical Properties of Metal Nanoparticles:
23 The Influence of Size, Shape, and Dielectric Environment. *J. Phys. Chem. B* **2003**, *107*, 668–677.
24
25
26 (29) Alonso-González, P.; Albella, P.; Neubrech, F.; Huck, C.; Chen, J.; Golmar, F.; Casanova, F.; Hueso, L. E.;
27 Pucci, A.; Aizpurua, J. et al. Experimental Verification of the Spectral Shift between Near- and Far-Field
28 Peak Intensities of Plasmonic Infrared Nanoantennas. *Phys. Rev. Lett.* **2013**, *110*, 203902.
29
30
31
32 (30) Bryant, G. W.; de Abajo, F. J. G.; Aizpurua, J. Mapping the Plasmon Resonances of Metallic
33 Nanoantennas. *Nano Lett.* **2008**, *8*, 631–636.
34
35
36
37 (31) Zuloaga, J.; Nordlander, P. On the Energy Shift between Near-Field and Far-Field Peak Intensities in
38 Localized Plasmon Systems. *Nano Lett.* **2011**, *11*, 1280–1283.
39
40
41 (32) Kats, M. A.; Yu, N.; Genevet, P.; Gaburro, Z.; Capasso, F. Effect of Radiation Damping on the Spectral
42 Response of Plasmonic Components. *Opt. Express* **2011**, *19*, 21748–21753.
43
44
45 (33) Moreno, F.; Albella, P.; Nieto-Vesperinas, M. Analysis of the Spectral Behavior of Localized Plasmon
46 Resonances in the Near- and Far-Field Regimes. *Langmuir* **2013**, *29*, 6715–6721.
47
48
49 (34) Picardi, G.; Colas, F. J.; Gillibert, R.; Lamy de la Chapelle, M. Spectral Shift of the Plasmon Resonance
50 Between the Optical Extinction and Absorption of Gold and Aluminum Nanodisks. *J. Phys. Chem. C*
51 **2016**,
52
53
54
55
56
57
58
59
60



TOC graphic

1
2
3
4
5
6
7
8
9
10
11
12
13
14
15
16
17
18
19
20
21
22
23
24
25
26
27
28
29
30
31
32
33
34
35
36
37
38
39
40
41
42
43
44
45
46
47
48
49
50
51
52
53
54
55
56
57
58
59
60